

Performance of Microfabricated Piezoelectric Vibration Energy Harvesters

Noël E. duToit^{1,2} and Brian L. Wardle¹

¹Department of Aeronautics and Astronautics, Massachusetts Institute of Technology,
77 Massachusetts Avenue, 33-314, Cambridge, MA 02139

Model verification and design of MEMS piezoelectric vibration energy harvesters (MPVEH) are presented, motivated by lowering power requirements of wireless sensor nodes. Applications include structural health monitoring. Coupled electromechanical harvester models are presented and verified (through comparison with experimental data). Harvester material selection is discussed. The model is used to concurrently design a prototype MPVEH and a microfabrication scheme. Targeting low-level (2.5 m/s^2), low-frequency (150 Hz) vibrations, power density ($310 \text{ } \mu\text{W/cm}^3$) and voltage ($0.4 \text{ } V_{p-p}$) are predicted. Methodologies for scalar analysis and optimization of harvesters are presented with a scheme for chip-level assembly of harvester clusters to meet node requirements.

Keywords: Energy scavenging; microelectromechanical systems (MEMS); piezoelectric; vibration energy conversion; microfabrication; model verification

INTRODUCTION

Distributed wireless micro-sensor networks, or systems of ubiquitous, low-cost, self-organizing agents (or nodes) [1], have been the research focus of multiple groups in recent years. These networks find application in many areas including building climate control, warehouse inventory and supply chain control, identification and personalization (RFID tags), the smart home [2], and structural health monitoring. A major concern for these node networks remain the power supply to each node [3].

The power requirement for these node networks has been driven down through advances in low power DSP's (Digital Signal Processors) and trends in VLSI (Very Large Scale Integration) system-design [4]. Power consumption of tens to hundreds of μW per node is predicted [2, 5-7]. The result is the possibility to develop self-powered sensor nodes. Power solutions envisioned for these self-powered nodes will convert ambient energy into usable electric energy, resulting in self-sustaining nodes.

Many ambient power sources (*e.g.*, thermal gradients, vibration, fluid flow, solar, *etc.*) have been investigated for long-term implementation of sensor node networks. Harvesting mechanical vibrations is a viable source of power, well matched to the needs of wireless sensor nodes. The conversion of ambient mechanical vibrations to electrical energy is the focus of the current research since mechanical vibrations occur pervasively in the environment. Specifically, a MEMS mechanical vibration energy harvester is investigated for its small size, low cost, and ease of implementation potential. In this paper, the coupled electromechanical device model is outlined (based on previous work), power is optimized, and model verification (comparison to experimental results) is briefly presented (refer to [8, 9] for a detailed derivation). Based on the presented modeling and the microfabrication of a high-level, high-frequency prototype device, a feasible fabrication scheme is presented for a 3-variable geometrically optimized prototype harvester.

²Currently Doctoral candidate at California Institute of Technology, Department of Mechanical Engineering

MODELING OF RESONANT ENERGY HARVESTERS: Modeling, Power Optimization, and Model Verification

Low-level mechanical vibrations occur pervasively in the environment [9] and high levels occur on machinery and vehicles such as automobiles or aircraft. A low-level mechanical vibration energy harvester is the focus of the current research. Such harvesting devices can be divided into two groups [10]: non-resonant and resonant energy harvesters (*i.e.*, device resonance frequency is matched to vibration input frequency). These devices are effective in different vibration regimes and are thus not competing configurations. The non-resonant energy harvester is more efficient where the input contains very low frequency (< 10 Hz), irregular vibrations with amplitudes larger than the device critical dimensions. This configuration finds application in human movement energy harvesters (for example with wearable computing applications [10-12]). Resonant energy harvesters find application where the input vibrations are regular, frequencies are higher (> 100 Hz), and the input vibration amplitude is smaller than the device critical dimensions. Regular vibrations are continuous with stable and well-defined vibration spectra, such as vibrations generated by an unbalanced machine. Resonant energy harvesters are the focus of the current research.

There are three methods of conversion from mechanical vibration energy to electrical energy: a variable capacitor (electrostatic), an inductor (electromagnetic), and by utilizing the piezoelectric effect. The piezoelectric effect has been found to be the most effective [13] of the three types (and is at a minimum competitive with electrostatic or electromagnetic conversion), it does not require the use of a transformer, and microfabrication schemes for thin-film piezoelectric ceramics are improving. Thus, the piezoelectric effect is utilized in the current research due to its advantages and compatibility with MEMS fabrication processes.

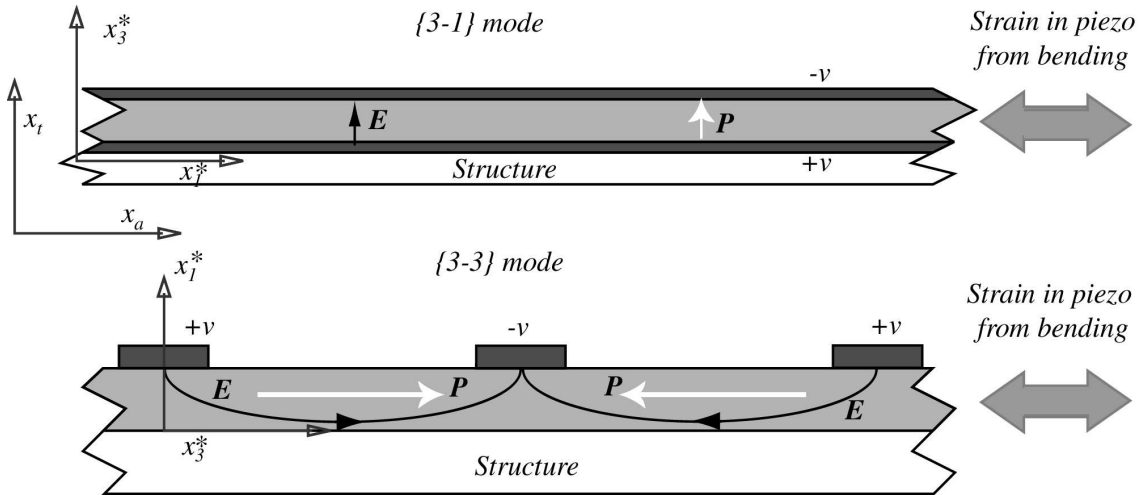


Figure 1. {3-1} (*top*) vs. {3-3} (*bottom*) mode of operation for resonant harvesters in bending. Local piezoelectric material coordinates (x_1^* , x_3^*) and global beam coordinates (x_a , x_t) are shown. E indicates the electric field, ν is voltage, and P is the poling direction.

The cantilever beam configuration was chosen for its geometric compatibility with the MEMS fabrication processes. It is also a relatively compliant structure, allowing for large strains needed for power generation. Two modes of operation are possible for this configuration: the {3-1}-mode and {3-3}-mode. These modes are illustrated in Figure 1 for the cantilever configuration. For the {3-1}-mode, the strain is applied perpendicular to the poling direction, whereas the strain is applied in the poling direction for the {3-3} mode of operation. The {3-3}-mode piezoelectric coupling is generally larger than the {3-1}-mode

coupling and is typically the preferred mode. For the {3-1}-mode, two harvester geometries can be used: uni-morph and bi-morph (refer to Figure 2). Only the uni-morph geometry is obtainable for the {3-3}-mode harvester due to microfabrication considerations associated with the interdigitated electrodes. Each harvester has the following components: the cantilevered beam structure, piezoelectric element(s), and electrodes. A proof mass can be added if necessary.

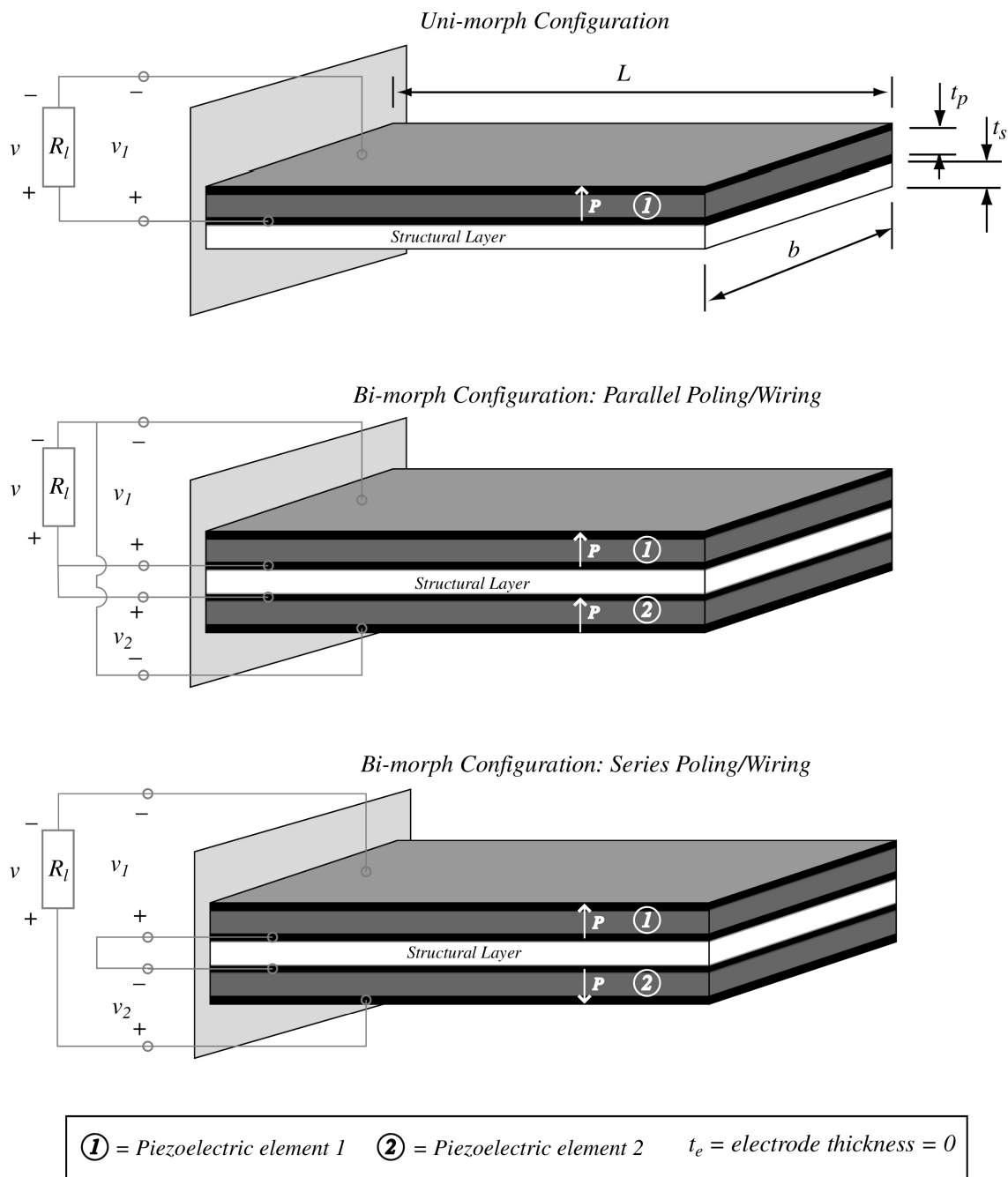


Figure 2. Cantilever (top) uni-morph and (middle/bottom) bi-morph configurations for {3-1} operation. R_l is the electrical load, b is the width of the structure, t is the layer thickness, L is the structure length, and v is the voltage developed.

Modeling

In prior work [8, 9], a coupled electromechanical model for a base-excited cantilever beam with a mass at the free end is presented. The model can be obtained with an energy method approach. The model is based on a modal decomposition of the mechanical response of the system combined with the small-signal linear constitutive law for piezoelectric materials. A detailed analysis of the relationship between poling direction, piezoelectric constants, and applied and developed electric fields is included in [8]. The piezoelectric local material coordinates (x_1^*, x_3^*) and global beam coordinates (x_a, x_t) are defined in Figure 1. For the modal analysis, the mechanical response (relative lateral motion) is written as the sum of nr individual mechanical mode-shapes, ψ_{r_i} , multiplied by the generalized mechanical coordinate, r_i , which is a function of time, t (according to the Raleigh-Ritz approach):

$$z(x_a, t) = \sum_{i=1}^{nr} \psi_{r_i}(x_a) r_i(t) = \boldsymbol{\Psi}_r(x_a) \mathbf{r}(t)$$

z is the beam neutral axis displacement relative to the input base displacement, w_B . In a similar fashion, the electrical response (voltage) is written in terms of nj electrical mode shapes, ψ_{v_j} , and the generalized electrical coordinate, v_j . The actuator and sensing, or governing, equations for multiple mechanical and electrical modes are obtained:

$$\mathbf{M}\ddot{\mathbf{r}} + \mathbf{C}\dot{\mathbf{r}} + \mathbf{K}\mathbf{r} - \boldsymbol{\Theta}\mathbf{v} = -\mathbf{B}_f \ddot{w}_B \quad (1)$$

$$\boldsymbol{\Theta}^t \mathbf{r} + \mathbf{C}_p \mathbf{v} + \mathbf{q} = \mathbf{0} \quad (2)$$

The overhead dot indicates a time derivative while the prime indicates a spatial derivative. Superscript t indicates the transpose of the vector or matrix. \ddot{w}_B is the absolute base input acceleration. The mass (\mathbf{M}), stiffness (\mathbf{K}), coupling ($\boldsymbol{\Theta}$), and capacitive matrices (\mathbf{C}_p) are defined from a variation of calculus analysis:

$$\mathbf{M} = \int_{V_s} \boldsymbol{\Psi}_r^t \rho_s \boldsymbol{\Psi}_r dV_s + \int_{V_p} \boldsymbol{\Psi}_r^t \rho_p \boldsymbol{\Psi}_r dV_p \quad (3)$$

$$\mathbf{K} = \int_{V_s} (-x_t \boldsymbol{\Psi}_r'')^t \mathbf{c}_s (-x_t \boldsymbol{\Psi}_r'') dV_s + \int_{V_p} (-x_t \boldsymbol{\Psi}_r'')^t \mathbf{c}^E (-x_t \boldsymbol{\Psi}_r'') dV_p \quad (4)$$

$$\boldsymbol{\Theta} = \int_{V_p} (-x_t \boldsymbol{\Psi}_r'')^t \mathbf{e}^t (-\nabla \boldsymbol{\Psi}_v) dV_p \quad (5)$$

$$\mathbf{C}_p = \int_{V_p} (-\nabla \boldsymbol{\Psi}_v)^t \boldsymbol{\varepsilon}^S (-\nabla \boldsymbol{\Psi}_v) dV_p \quad (6)$$

Here, V indicates the element volume, and subscript s is the structural section while subscript p indicates the active element. \mathbf{c} is the stiffness, \mathbf{e} is the piezoelectric constant, and $\boldsymbol{\varepsilon}$ is the permittivity matrix. Superscript S indicates the piezoelectric property analyzed at constant strain while superscript E indicates the piezoelectric material property analyzed at constant electric field (*i.e.*, short-circuited). \mathbf{q} is the charge and reduces to a column vector with values equal to the total charge developed in the system. The forcing vector, \mathbf{B}_f , is due to the inertial loading over the length (L) of the structure and is defined in terms of the mass per length, m :

$$\mathbf{B}_f = \int_0^L m(x_a) \boldsymbol{\Psi}_r' dx_a = m \int_0^L \boldsymbol{\Psi}_r' dx_a \quad (7)$$

Power Optimization

Much insight is gained when the resulting matrix governing equations (eqs. (1) and (2)) are simplified by considering one beam mode and a single electrode pair, thus

approximating the infinite degree-of-freedom mechanical system as a single-degree-of-freedom system. The governing equations reduce to scalar equations, which allows for an extracted power optimization to be performed. A scheme to reduce a device with multiple piezoelectric elements to an equivalent system with a single piezoelectric element is detailed in [8] (as is necessary for bi-morph harvesters). The scalar actuator equation is written in an alternative form by dividing through by M and making use of the definitions for the first resonance frequency, $\omega_1 = \sqrt{k/M}$, and damping ratio $\zeta_m = \frac{c}{2M\omega_1}$. Note that, since one vibration mode is considered ($\psi_r = \psi_{r1}$), the system will have a single natural frequency (one degree of freedom). For a structure with an active/piezoelectric component, the natural frequency will correspond to either the resonance or anti-resonance frequency, depending on the electrical loading (short- or open-circuit). $\omega_r = \omega_1$ corresponds to the resonance frequency. In the scalar sensing equation, the charge can be related to the voltage through $v = \frac{dq}{dt} R_l = iR_l$ to obtain the scalar governing equations:

$$\ddot{r} + 2\zeta_m \omega_1 \dot{r} + \omega_1^2 r - \frac{\theta}{M} v = -\frac{B_f}{M} \ddot{w}_B \quad (8)$$

$$\theta \dot{r} + C_p \dot{v} + \frac{1}{R_l} v = 0 \quad (9)$$

Dimensionless factors ($\alpha = \omega_1 R_l C_p$, $\kappa^2 = \frac{\theta^2}{KC_p}$, and $\Omega = \frac{\omega}{\omega_1}$) are defined. ω is the base input frequency, α is the dimensionless time constant and κ^2 is a structure/system electromechanical coupling coefficient. The system response and power are calculated as:

$$\left| \frac{r}{B_f \ddot{w}_B} \right| = \frac{1}{K} \frac{\sqrt{1 + (\alpha\Omega)^2}}{\sqrt{[1 - (1 + 2\zeta_m \alpha)\Omega^2]^2 + [(2\zeta_m + \{1 + \kappa^2\}\alpha)\Omega - \alpha\Omega^3]^2}} \quad (10)$$

$$\left| \frac{v}{B_f \ddot{w}_B} \right| = \frac{1}{|\theta|} \frac{\alpha\kappa^2 \Omega}{\sqrt{[1 - (1 + 2\zeta_m \alpha)\Omega^2]^2 + [(2\zeta_m + \{1 + \kappa^2\}\alpha)\Omega - \alpha\Omega^3]^2}} \quad (11)$$

$$\left| \frac{P_{out}}{(B_f \ddot{w}_B)^2} \right| = \frac{\omega_1}{K} \frac{\alpha\kappa^2 \Omega^2}{[1 - (1 + 2\zeta_m \alpha)\Omega^2]^2 + [(2\zeta_m + \{1 + \kappa^2\}\alpha)\Omega - \alpha\Omega^3]^2} \quad (12)$$

Eq. (10) gives the generalized mechanical displacement (modal analysis [9]), which can be converted to actual displacements by multiplying it with the mode shape (eq. (1)). The next step is to optimize the power extracted, which is detailed in [8], and is merely outlined here. The system can be analyzed at short- and open- circuit conditions by letting the electrical load resistance tending to zero and infinity, respectively. Two optimal frequency ratios for maximum power generation are obtained, which correspond to the resonance (subscript r) and anti-resonance (subscript ar) frequencies of the beam structure:

$$\Omega_r = 1 \text{ and } \Omega_{ar} = \sqrt{1 + \kappa^2} \quad (14)$$

The anti-resonance frequency (ω_{ar}) is determined by the coupling term $\kappa^2 = \frac{\theta^2}{KC_p}$.

The structure is made up of both active and inactive layers, resulting in a two-part stiffness term (K) (refer to eq. (4)). As a result, the coupling term does not correspond solely to the material coupling coefficient. At the macro-scale, the active element contributes negligibly to the overall stiffness of the structure for most harvesting applications. For this reason, the change in natural frequency from resonance to anti-resonance is often indistinguishable. However, at the micro-scale the active element often constitutes the majority of the structure, and the shift from resonance to anti-resonance frequency is much more pronounced.

The power can further be optimized with respect to load resistance to obtain an optimal electrical load. This is achieved by optimizing the power with respect to the dimensionless time constant, α :

$$\alpha_{opt}^2 = \frac{1}{\Omega^2} \frac{(1 - \Omega^2)^2 + (2\zeta_m \Omega)^2}{([1 + \kappa^2] - \Omega^2)^2 + (2\zeta_m \Omega)^2} \quad (15)$$

Next, the optimal time constant (or electrical load) and frequency are substituted back into power equation (12). For MEMS-scale devices, ζ_m is generally at least an order of magnitude smaller than κ^2 . With this assumption, the power equation is approximated as eq. (16) at both the resonance and anti-resonance frequencies (under optimal electrical load):

$$\left| \frac{P_{out}}{(B_f \ddot{w}_B)^2} \right|_{opt} \approx \frac{\omega_1}{K} \frac{1}{8 \zeta_m} \quad \text{or} \quad |P_{out}|_{opt} \approx \frac{B_f^2}{\sqrt{KM}} \frac{\ddot{w}_B^2}{8 \zeta_m} \quad (16)$$

This results suggest that the power extracted under optimal conditions at the two optimal frequencies (resonance and anti-resonance, respectively) are equal. Secondly, the piezoelectric coupling cancels from the power equation under optimal conditions. In fact, the only material properties that affect the maximum power developed are the density and stiffness (short-circuit for the active material). This is a counterintuitive result which suggests that the specific active material used (*e.g.*, PZT-5A vs. PZT-5H) has no effect on maximum power developed (under optimal conditions). This finding will be discussed in more detail in Section 3.

Model Verification

Model verification has been undertaken by comparing simulated and measured response for an experimental device [8, 14]. Details of the model verification will be presented elsewhere [14] with a brief summary given here. The measured and simulated results for a bi-morph {3-1} series-connected cantilever device are presented in Figure 3, plotting power vs. frequency for six electrical loads. As can be seen in Figure 3, the model predicted the overall response of the system very well, including the resonance and anti-resonance frequencies, and the corresponding optimal electrical resistances (for maximum power extraction). Off-resonance prediction of mechanical (displacement) and electrical (voltage, power) parameters are in excellent agreement. At the resonances, the simulations consistently underpredicted the electrical performance (power underprediction at resonances is visible in Figure 3). The higher measured values are attributed to the non-linear response of the piezoelectric element to applied strain [15]. Independent experiments verify this attribution [14]. At higher applied strain conditions, the piezoelectric constant is higher than assumed with the small-signal linear model. Thus, a higher electric field is induced, resulting in both higher voltages and higher power generation.

Based on these results, it was concluded that the model accurately represents the physical system away from resonance. Around the resonances, the model consistently underpredicts the electrical performance of the device due to piezoelectric material non-linearity. Thus, when applying the model for design purposes, it can be expected that the device will produce slightly more power (a factor of <2) at the resonances.

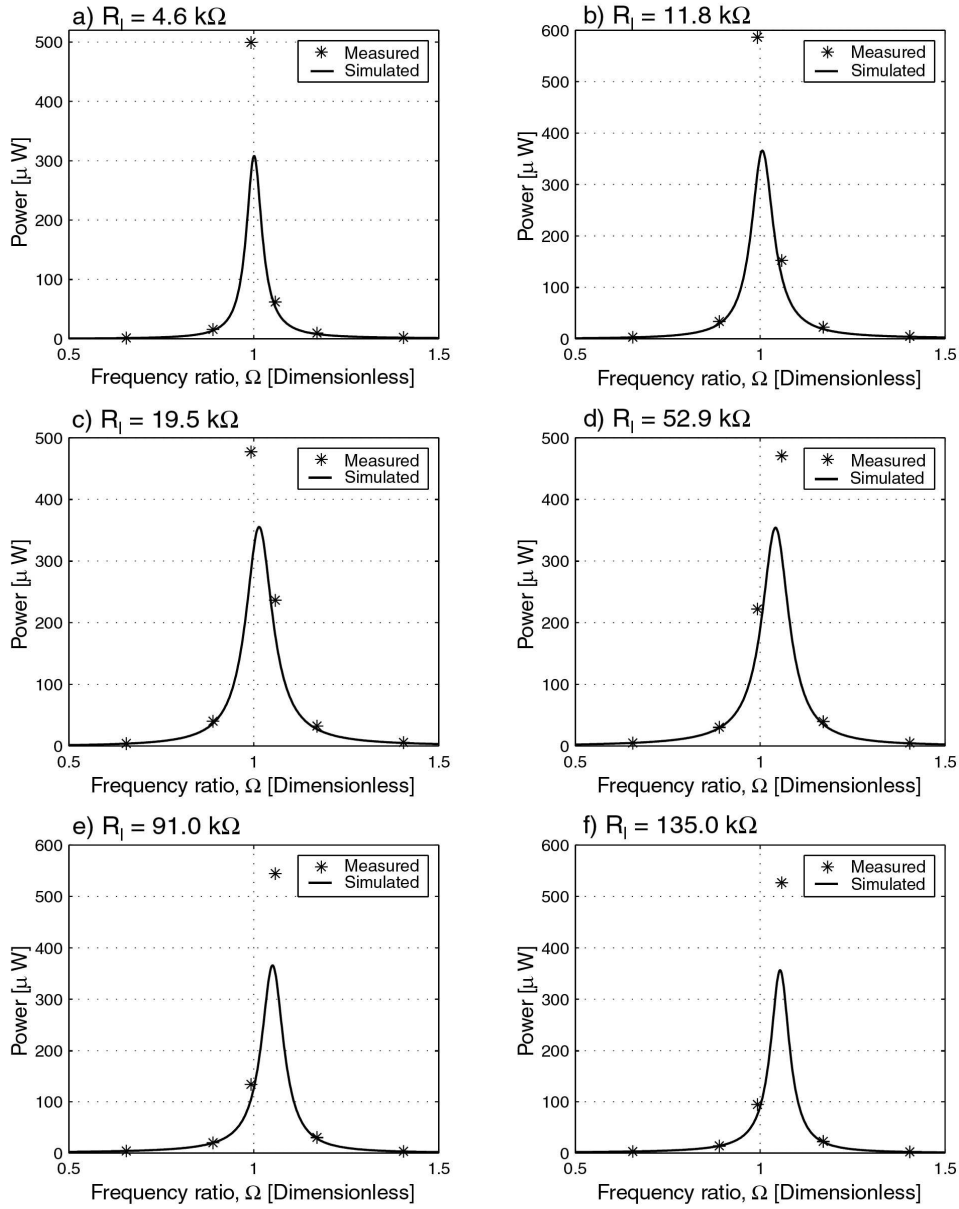


Figure 3. Predicted vs. measured power plotted vs. frequency for varying electrical loads. Base acceleration is held constant at 2.5 m/s^2 . $f_r = 107 \text{ Hz}$ and $f_{ar} = 113 \text{ Hz}$.

MEMS HARVESTER DESIGN IMPLICATIONS FROM MODELING AND MICROFABRICATION INVESTIGATIONS

Based on the modeling and optimization results, combined with the fabrication of a high-level, high-frequency prototype device [16, 17], certain MEMS design implications are identified, as discussed next.

At the MEMS-scale, electromechanical coupling is dependent on both the active and the structural layers. Also, an analysis of the dominant damping terms at various scales and under different operating conditions reveals macro- vs. MEMS-scale differences [8, 9]. Results indicate that the scheme implemented when choosing an input frequency (from the vibration spectrum of the source) should be adapted to account for the frequency dependence of the dominant damping term whereas at the macro-scale structural/material damping dominates. At the micro-scale, viscous damping is the dominating damping term. Furthermore, there exist two operating frequencies (resonance and anti-resonance), with corresponding electrical loads (short and open-circuit, respectively). At both these points the maximum power can be extracted, but voltage and current differs greatly [9]. At resonance, a high current is developed, compared to a high voltage at the anti-resonance frequency. The operating point selection should be made, based on the specific application. For example, charging a secondary battery requires a high current, while diodes and transistors require relatively high voltages to operate. Secondly, eq. (16) showed that, when the harvester is operated at either of the optimal operating points, *under optimal electrical loads* (e.g., the maximum power is generated), the piezoelectric coupling cancels out of the equation. This is true if the coupling term, κ^2 , is much larger than the mechanical damping, ζ_m . The only material properties that affect the power generated are the density and the bending modulus of the total device. The density should be maximized, while the elastic stiffness should be minimized. This simple result implies the following: solely considering maximum power generation, the mode of operation ({3-1} vs. {3-3}) has very little effect on the power generated. The material density is independent of orientation, and the difference between the modulus, parallel and perpendicular to the poling direction, respectively, is small for common piezoelectrics/poled ferroelectrics, e.g., PZT-5A vs. PZT-5H. Thus, the maximum power generated is largely independent of piezoelectric coupling and mode of operation, assuming that the same geometry is obtainable for both operational modes. This is illustrated quantitatively in Table 1 for two devices made from two materials (PZT-5A and PZT-5H). In this example, power generation is the same despite large differences in the piezoelectric material properties. The optimal electrical loads and actual electrical performance are quite different.

Conversely, both the material selection and the mode of operation will determine the voltages and currents developed in the device. The voltage developed at optimal power extraction is inversely proportional to the piezoelectric constant, whereas the current is proportional to this coefficient [8, 9]. One of the advantages of using the {3-3}-mode of operation is that the output voltage can be controlled. This voltage is determined by the spacing between the electrodes. Since interdigitated electrodes are used for this mode of operation [9], the pitch between the electrodes can be varied to obtain the required voltage. It is important to note that the {3-3}-mode harvester necessitates a uni-morph configuration due to the microfabrication process currently used and the shape of the electrodes. Thus, the resulting structure has an asymmetric geometry. The asymmetric geometry necessitates the use of structural layers to ensure that the (single) piezoelectric element is above the neutral axis of the structure (to prevent strain cancellation). In general, these structural layers are silicon based, which are less dense and stiffer (higher bending stiffness) than the piezoelectric layer, both characteristics that are detrimental to power generation. Perhaps the most important practical consideration for this type of device (cantilevered structure) is the residual stress. For low frequency devices, high aspect ratios are required to obtain the low resonance frequency, and as such the residual stress in the cantilevered structure is of concern. The asymmetric geometry for the {3-3}-mode harvester results in a moment imbalance and the released structure tends to curl upon release.

TABLE I. Power prediction using PZT-5A and PZT-5H piezoelectric ceramics, respectively. Device geometry as presented in Table 4, base acceleration = 2.5 m/s^2 at 150 Hz.

Material Property	PZT-5A	PZT-5H
$s_{11}^E [m^2/N]$	16.4×10^{-12}	16.5×10^{-12}
$s_{12}^E [m^2/N]$	-5.74×10^{-12}	-4.78×10^{-12}
$c_{11}^E * [N/m^2]$	69.5×10^9	66.2×10^9
$d_{31} [N/m^2]$	-171×10^{-12}	-274×10^{-12}
$e_{31} * [C/m^2]$	-16.0	-23.4
$\epsilon_{33}^T [F/m]$	$1700 \times \epsilon_0$	$3400 \times \epsilon_0$
$\epsilon_{33}^S * [F/m]$	$1080 \times \epsilon_0$	$1953 \times \epsilon_0$
$\rho_p [kg/m^3]$	7750	7500
Resonance operation		
Resonance frequency [Hz]	145.8	145
Optimal electrical load [$k\Omega$]	7.7	3.6
Power density [$\mu W/cm^3$]	74.0	74.0
Voltage developed [V]	0.03	0.02
Current developed [μA]	4.1	5.9
Anti-resonance operation		
Anti-resonance frequency [Hz]	150.2	150.2
Optimal electrical load [$k\Omega$]	281	183
Power density [$\mu W/cm^3$]	74.0	74.0
Voltage developed [V]	0.19	0.15
Current developed [μA]	0.67	0.83

* Refers to plate effective properties.

In the case of the {3-1}-mode of operation, the thickness of the piezoelectric layers determines the voltage output. However, the active element thickness also influences dynamics of the structure, and is limited by the fabrication process. On the other hand, the {3-1}-mode devices allow for a symmetric bi-morph configuration to be utilized. This has three effects:

- First, the electrical output (voltage and current) from the bi-morph device can be controlled through the two possible electrical configurations: series and parallel ‘connections’ depending on the poling direction [8]. To avoid confusion in the sections to follow, *series poling* will refer to the configuration where the two active elements are poled such that the two elements are wired in series (Figure 2, bottom). Likewise, *parallel poling* refers to the poling condition where the two active elements are wired in parallel (Figure 2, middle). Thus, parallel and series poling refer to electrical characteristics of *single* devices. For series poling, the voltages add, and the current developed through the two elements is constant (refer to Figure 4). For parallel poling, the currents add and the voltages are constant. It is possible to reduce this multiple electrode system into an equivalent single electrical degree-of-freedom system (with one effective active element), which is detailed in [8]. The resulting equivalent system has scalar governing equations, which can be optimized as in Section 2.2.

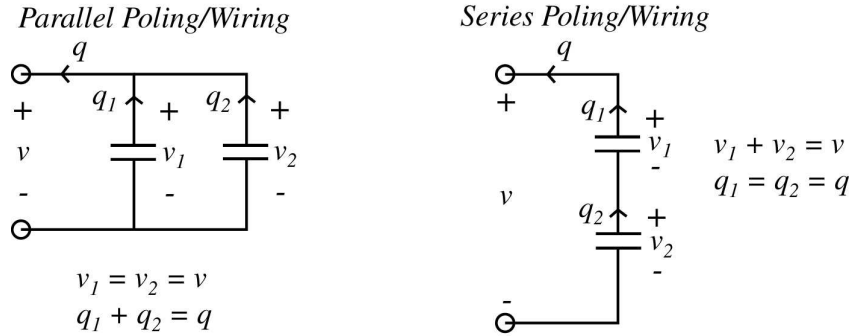


Figure 4. Bi-morph configuration simplified effective electrical circuit for the (*left*) parallel and (*right*) series poling. The two piezoelectric elements are represented as simple capacitors. See Figure 2 for device wiring configuration.

- Second, a symmetric structure can be obtained. This is very beneficial in the attempt to limit the residual stress, or as in this case, the effect of the residual stresses upon the release of the structure. Note that thin-film PZT microfabrication attempts have not been able to achieve a MEMS bi-morph due to issues with PZT sol-gel processes of building subsequent PZT layers on top of electrodes. A uni-morph harvester is the single example of a MEMS harvester fabricated and tested [16-18]. A fabrication scheme for a bi-morph MEMS harvester is presented in the next section, but clearly process development is necessary to realize such a device. Since the bi-morph configuration is very desirable (discussed above) such a design is further analyzed to illustrate the potential of such a device.
- Thirdly, the bi-morph configuration eliminates the need for a structural layer, and more volume of the device can consist of the denser, more compliant piezoelectric material (as compared to the silicon-based structural layers required for the {3-3}-mode harvester), which would increase the overall efficiency of harvested power. Lastly, the lack of control of the voltage in {3-1}-mode harvesters due to the layer thickness limitation is offset by the relative ease with which these individual devices can be interconnected (either in series or in parallel) on a die to form a cluster of harvesters. Henceforth, *parallel-* or *series-connection* will refer to the electrical manner in which individual bi-morph devices are connected to each other to form clusters at the chip level. The parallel connection is preferred when considering the chip-level fabrication where individual devices are connected to one another [8]. Refer to Figure 5 for an illustration of three *parallel-poled* individual devices in a *parallel connection*.

Based on these considerations, a bi-morph device utilizing the {3-1} mode of operation is selected for optimal design since the marginal benefit of using the {3-3} mode of operation is offset by the added complexity in the fabrication of the device and/or reduced power density due to the resulting geometry of the device.

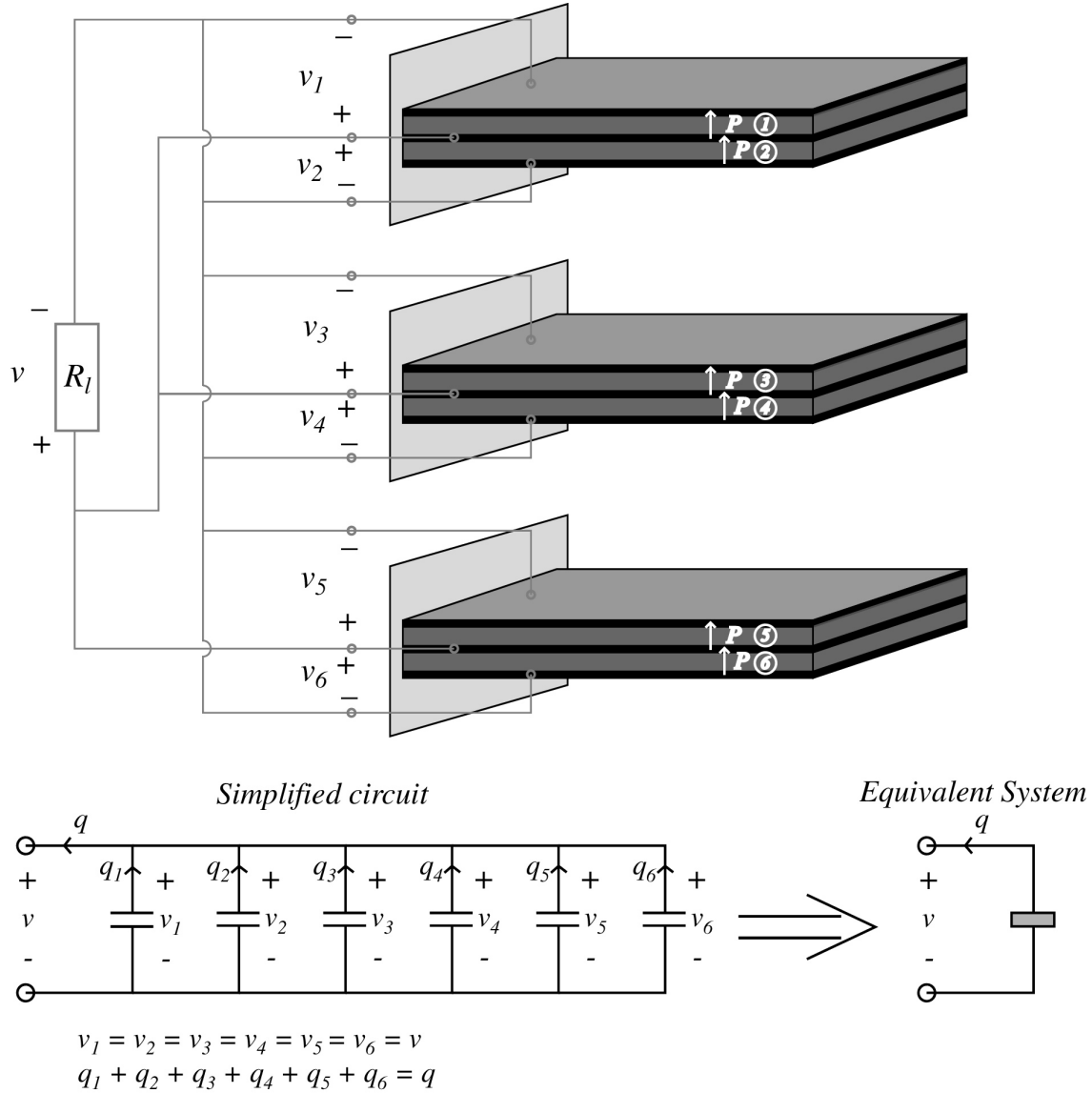


Figure 5. Cluster made up of 3 parallel-poled individual harvesters: (top) interconnected in parallel (parallel connection) to additively collect current /charge and (bottom) a simplified parallel-circuit representation for the 3-harvester cluster.

PROTOTYPE DESIGN AND MICROFABRICATION SCHEME: Architecture Selection and Microfabrication and Optimal Design under Constraints

A cantilever beam configuration was chosen for its simplicity, compatibility with MEMS manufacturing processes, and its low structural stiffness. A low resonant frequency is desired since the ambient vibration measurements have shown that the majority of ambient sources have significant vibration components below 300 Hz [8, 9]. However, designing a MEMS device with the resonant frequency below 100 Hz can be problematic [13]. For this illustrative design, an input frequency of 150 Hz was assumed, with a base acceleration of 2.5 m/s² (approximately that of a microwave oven side panel).

Architecture Selection and Microfabrication

As mentioned, the parallel connection for the bi-morph structure is preferred from fabrication considerations. A {3-1}-mode bi-morph parallel-poled and parallel-connection cluster is selected. The voltage developed for an individual harvester with parallel poling is half of the voltage developed for the series connection (refer to Figure 4), assuming the structures are identical and operate in phase (perhaps through the inclusion of tethers between the structures). The converse is true for the current. To generate higher voltage the anti-resonance frequency of the single device is aligned with the frequency of vibration input (150 *Hz*). However, the current developed at this operating point is very low. This can be somewhat addressed by connecting the bi-morph devices in parallel (parallel connection). The concept is illustrated for three bi-morph harvesters (one cluster) in Figure 5. The proposed fabrication scheme to achieve this geometry (a cluster of three parallel-poled bi-morph devices connected in parallel) is described below. Finally, it is possible to connect a number of these clusters to form a chip-level device. By changing the number of harvesters in the clusters, and the number of clusters on the chip-level device, the electrical output from the system can be controlled.

To fabricate the 3-harvester (parallel-poled and parallel-connected) cluster (clusters connected in series as an example here), a total of four masks would be required. The substrate used for the process is an N-type <100>, 6 inch silicon wafer (~500 μm thick). Standard substrate specifications include: double-sided polished, total thickness variation < 3 μm , bow and wrap < 10 μm . Refer to Figure 6 for a graphical illustration of the major process steps. The first step is to deposit an insulating oxide layer (PECVD). This is to electrically insulate the device from the conducting substrate. Next, the bottom electrodes (titanium and platinum) are deposited via electron-beam deposition and annealed. The first of the PZT layers are deposited with a sol-gel spin-on process, including baking and anneal steps. The process is repeated until the desired PZT thickness is obtained. Next, the center electrode is deposited (electron-beam deposition) and annealed. The second PZT layer is deposited as before, and lastly, the top electrode layer is deposited (see Figure 6, top). The device is coated with a thick photo-resist and patterned with the first mask and then ion-milled (timed) to define the device layout (Figure 6, second from top). Two more patterning (masks 2 and 3) and ion-milling steps expose the bottom and center electrodes, respectively. Next, the substrate is turned over and is polished down to 200 μm thickness, using Chemical Mechanical Polishing (CMP). The substrate is patterned using mask 4. The device is released and the proof mass is defined with a DRIE (Deep Reactive Ion Etching) step. The oxide layer is also etched and the bottom electrode acts as an etch stop. A symmetric, bi-morph configuration is obtained. Refer to Figure 6, second from bottom, for an illustration of the released structure. The plan-form view of a cluster of three devices (parallel connection) is shown at the bottom of Figure 6.

Post-processing steps include, among others, the non-trivial separation of the dies to form devices. The harvester clusters will have to be interconnected using bond-pads created above to finish the chip-level harvester. All the devices within a cluster are interconnected as required (a consequence of the process developed). When the device is eventually packaged, the substrate will have to be supported. The final device will have two connections to be connected to the load or storage device. Lastly, tethers between the ends of the devices (not included here) may be possible to ensure in-phase operation of the harvesters in the clusters.

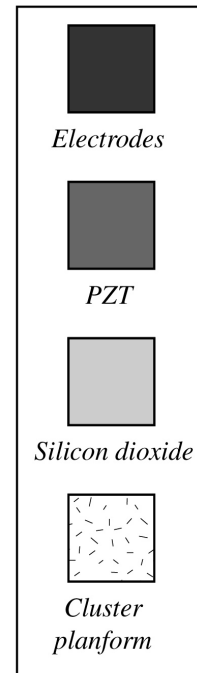
Oxide, three electrode layers, and two PZT layers.



Structure defined through ion milling.



Structured released with DRIE backside etch.



Planform of harvester cluster (wire-bond connections also indicated).

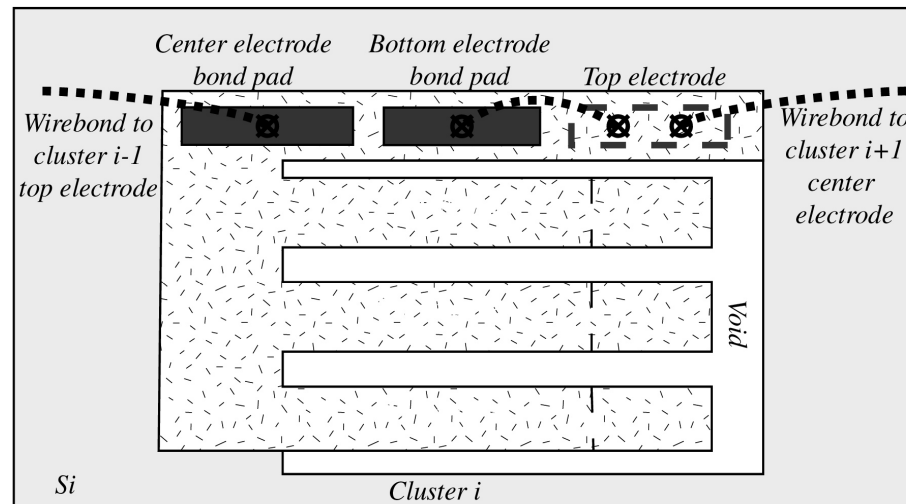


Figure 6. Illustration of fabrication scheme: (top) single device cross-sections at various fabrication steps and (bottom) planform of 3-harvester cluster, including wire-bond connections (clusters connected in series) to adjacent clusters.

A constraint imposed by the MEMS manufacturing processes is the limitation on the cantilevered structure length to around 1 *mm* (length to thickness ratio, $\sim 1000 : 1$), such that a proof mass is needed to reduce the natural frequency of the device further. Both the power and volume are proportional to the width, so the width does not affect the power density of the individual harvester. This variable does however affect the current developed, as well as the power developed per harvester. The width is approximately limited to 2 *mm*. A maximum allowable strain of 500 μ -strain has been assumed, which is conservative (2,000 μ -strain fatigue limit has been reported for sol-gel deposited PZT). This limit is imposed to both prevent depoling of the piezoelectric elements [19], and to prevent static failure. Mechanical fatigue in MEMS devices is normally negligible [20, 21], however, fatigue will be considered in future work.

Optimal Design under Constraints

The constraints for the optimization are summarized in Table 2.

TABLE II. Constraints for MPVEH prototype device design optimization.

Constraint	Motivation
Geometric constraints	
$0 < L < 1.0 \text{ mm}$	The cantilevered structure length was limited due to microfabrication considerations.
$0.1 < t_p < 1.0 \text{ }\mu\text{m}$	Limits enforced by spin-on process used for deposition.
$0 < L_0 < 1.0 \text{ mm}$	Proof mass length limit from microfabrication considerations.
Material constraints	
$S_1 < 500 \text{ }\mu\text{-strain}$	Limited to prevent depoling of the piezoelectric element [19].
Device level constraints	
$149 < f_{\text{ar}} < 150 \text{ Hz}$	Anti-resonance frequency of 150 <i>Hz</i> is required.
$L + L_0 < 1.0 \text{ mm}$	Total structure length limited.

Material properties are required for the device layers. For the piezoelectric layers, PZT-5A properties were assumed (refer to Table 1) based on prior work using the sol-gel PZT [16-18]. Additional material properties are summarized in Table 3, along with the properties for the other materials in the cantilever. It was assumed that the two PZT layers are of equal thickness. The same assumption was made for the titanium ($t_{ti} = 0.02 \text{ }\mu\text{m}$) and platinum layers thicknesses ($t_{pt} = 0.1 \text{ }\mu\text{m}$). Lastly, the proof mass will consist of silicon for the current manufacturing scheme.

Using the material properties (Tables 1 and 3) and imposing the constraints due to the fabrication processes (Table 2) on the optimization, the geometry (three variables only: cantilever length, PZT thickness, and proof mass length) is optimized to maximize the power. It should be noted that the limiting constraint on the developed power and the mechanical response of the device is the maximum allowable strain and not the geometric constraint imposed by the microfabrication processes. Since the strain is directly related to the quality factor, the optimal design is a function of both the mechanical damping (which is related to the quality factor) and the input vibration. The damping is dependent on the geometry and the operating environment of the device. Thus, an iterative design optimization will be required, based on more accurate damping and maximum allowable strain data. An illustrative optimal design is given in Table 4, including a summary of the predicted performance at the anti-resonance frequency. A base acceleration of 2.5 m/s^2 at 150 *Hz* and a mechanical damping ratio of $\zeta_m = 0.005$ [18] has been assumed (with the strain constraint described above).

TABLE III. Material properties used for MPVEH prototype device design optimization (in addition to those in Table 1 for PZT-5A).

Property	Value	Reference
Electrode material properties: Platinum (pt)		
c_{pt} [N/m^2]	170×10^9	[22]
ν_{pt}	0.39	[23]
ρ_{pt} [kg/m^3]	21,440	[23]
c_{pt}^* [N/m^2]	200.5×10^9	Plate stiffness
Electrode material properties: Titanium (ti)		
c_{ti} [N/m^2]	110×10^9	[22]
ν_{ti}	0.34	[23]
ρ_{ti} [kg/m^3]	4,510	[23]
c_{ti}^* [N/m^2]	124.4×10^9	Plate stiffness
Proof mass material properties: Silicon		
ρ_0 [kg/m^3]	2,330	[23]

* Refers to plate effective property.

TABLE IV. Optimized single MPVEH harvester design and predicted performance.

Geometric Parameter	Value	Performance Parameter (Anti-resonance design)	Value
*Structure length, L [mm]	0.860	Resonance frequency [Hz]	146
Structure width, b [mm]	2.00	Anti-resonance frequency [Hz]	150
*Piezo thickness, t_p [μm]	0.360	Maximum power § [μW]	0.126
Platinum thickness, t_{pt} [μm]	0.100	Optimal electrical load [$k\Omega$]	281
Titanium thickness, t_{ti} [μm]	0.020	Voltage developed [V]	± 0.188
*Proof mass length, L_0 [mm]	0.139	Current developed [μA]	0.670
Proof mass width, b_0 [mm]	2.00	Maximum strain [μ -strain]	± 500
Proof mass height, t_0 [μm]	200	Tip displacement [μm]	± 299
Foot-print area † [mm^2]	2.00	Power density † [$\mu W/cm^2$]	6.30
Harvester volume ‡ [mm^3]	0.402	Power density ‡ [$\mu W/cm^3$]	313
Operating Volume $^{\infty}$ [mm^3]	1.68	Power density $^{\infty}$ [$\mu W/cm^3$]	75.0

§ Performance parameter optimized.

* Geometric property varied in optimization.

† Calculated from the foot-print area of a single device.

‡ Calculated from volume of a single device.

$^{\infty}$ Calculated from operating volume of a single device.

CONCLUSIONS

The design of a prototype low-level MEMS vibration energy harvester was undertaken. First, the design implications from the developed model and power optimization, combined with microfabrication considerations are presented. The device geometry and a fabrication scheme for the low-frequency prototype device is presented, which was concurrently developed with a suitable device geometry. Based on the limitations imposed by

the fabrication scheme, a 3-variable single device geometric optimization was performed. It was found that the device performance (maximum power) and design is largely governed by the maximum allowable strain in the device. The design optimization is dependent on the quality factor and the vibration input parameters used for the specific device considered here, and re-analysis will be necessary when these conditions or the device configuration change. The predicted power density of the single MPVEH prototype harvester is $313 \mu\text{W}/\text{cm}^3$ (normalized by the device volume) at 0.38 V peak-to-peak from a base acceleration of 2.5 m/s^2 at 150 Hz. Last, a scheme to control the electrical output of the chip-level harvester device (consisting of an assemblage of clusters of individual harvesters) is presented.

Future work includes design with other optimization functions (e.g., power density), as well as an extension of the optimization scheme to include more variables. The maximum power independence of piezoelectric material selection will be verified experimentally, and microfabrication of a MEMS uni-morph harvester will be undertaken. Experimental verification of the MEMS-scale harvester design and predictions is currently underway.

REFERENCES

- [1] E. Welsh, W. Fish, and J. P. Frantz, "Gnomes: A testbed for low power heterogeneous wireless sensor networks," Bangkok, Thailand, 2003.
- [2] J. M. Rabaey, M. J. Ammer, J. L. da Silva, Jr., D. Patel, and S. Roundy, "PicoRadio supports ad hoc ultra-low power wireless networking," *Computer*, vol. 33, pp. 42-48, 2000.
- [3] S. Roundy, P. K. Wright, and J. Rabaey, *Energy Scavenging for Wireless Sensor Networks with special focus on Vibrations*. Norwell, MA: Kluwer Academic Publishers, 2004.
- [4] S. Meninger, J. O. Mur-Miranda, R. Amirtharajah, A. Chandrakasan, and J. Lang, "Vibration-to-electric energy conversion," *Proceedings of the International Symposium on Low Power Electronics and Design, Digest of Technical Papers*, pp. 48-53, 1999.
- [5] R. Amirtharajah and A. P. Chandrakasan, "Self-powered signal processing using vibration-based power generation," *IEEE Journal of Solid-State Circuits*, vol. 33, pp. 687-695, 1998.
- [6] A. Chandrakasan, R. Amirtharajah, J. Goodman, and W. Rabiner, "Trends in low power digital signal processing," Monterey, CA, USA, 1998.
- [7] J. M. Rabaey, J. Ammer, T. Karalar, S. Li, B. Otis, M. Sheets, and T. Tuan, "PicoRadios for wireless sensor networks: The next challenge in ultra-low-power design," San Francisco, CA, 2002.
- [8] N. E. duToit, "Modeling and Design of a MEMS Piezoelectric Vibration Energy Harvester," S.M. Thesis in *Aeronautics and Astronautics*, Massachusetts Institute of Technology, Cambridge, MA: 2005, pp. 244.
- [9] N. E. duToit, B. L. Wardle, and S. G. Kim, "Design Considerations for MEMS-scale Piezoelectric Mechanical Vibration Energy Harvesters," *Integrated Ferroelectrics*, vol. 71, pp. 121-160, 2005.
- [10] P. D. Mitcheson, B. Stark, P. Miao, E. M. Yeatman, A. S. Holmes, and T. C. Green, "Analysis and optimization of MEMS electrostatic on-chip power supply for self-powering of slow-sensors" presented at Eurosensors, Portugal, 2003.
- [11] P. Miao, A. S. Holmes, E. M. Yeatman, T. C. Green, and P. D. Mitcheson, "Micro-machined variable capacitors for power generation," Edinburgh, United Kingdom, 2004.

- [12] T. von Buren, P. Lukowicz, and G. Troster, "Kinetic energy powered computing - an experimental feasibility study," 2003.
- [13] S. Roundy, P. K. Wright, and J. Rabaey, "A study of low level vibrations as a power source for wireless sensor nodes," *Computer Communications*, vol. 26, pp. 1131-1144, 2003.
- [14] N. E. duToit and B. L. Wardle, "Experimental verification of a coupled electromechanical model for MEMS piezoelectric vibration energy harvesters," presented at Accepted to 47th AIAA/ASME/ASCE/AHS/ASC Structures, Structural Dynamics, and Materials Conference, Newport, RI, 2006.
- [15] E. F. Crawley and E. H. Anderson, "Detailed models of piezoceramic actuation of beams," *Journal of Intelligent Materials Systems and Structures*, vol. 1, pp. 4-25, 1990.
- [16] Y. B. Jeon, R. Sood, J. H. Jeong, and S. G. Kim, "MEMS power generator with transverse mode thin film PZT," *Sensors and Actuators, A: Physical*, vol. 122, pp. 16-22, 2005.
- [17] R. Sood, Y. B. Jeon, J. H. Jeong, and S. G. Kim, "Piezoelectric micro power generator for energy harvesting," presented at Solid-State Sensor and Actuator Workshop, Hilton Head, SC, 2004.
- [18] R. Sood, "Piezoelectric Micro Power Generator (PMPG): A MEMS-based Energy Scavenger," in *Mechanical Engineering*, vol. S.M. Cambridge, MA: Massachusetts Institute of Technology, 2003, pp. 110.
- [19] K. Maki, N. Soyama, S. Mori, and K. Ogi, "Evaluation of CSD-PZT thick films with different film density," Honolulu, HI, 2000.
- [20] W. N. Sharpe Jr and J. Bagdahn, "Fatigue testing of polysilicon - A review," *Mechanics of Materials*, vol. 36, pp. 3-11, 2004.
- [21] S. M. Spearing, "Materials issues in microelectromechanical systems (MEMS)," *Acta Materialia*, vol. 48, pp. 179-196, 2000.
- [22] www.memsnet.org, 2005.
- [23] www.matweb.com, 2005.